



Cite this: DOI: 10.1039/d5cp04955e

Strong band bowing in BiOX (X = Cl, Br, I) due to halogen alloying

 Hai-Chen Wang,^a Aude Vives,^b Miguel A. L. Marques,^{a*} Clement Larquet^b and Jérôme Gomar^b

Bismuth oxyhalides (BiOX, X = Cl, Br, and I) are promising photocatalytic materials whose electronic and optical properties can be systematically tuned through halogen alloying. This study presents a comprehensive computational and experimental investigation of halogen anion alloying effects on the electronic structure and optical properties of BiOCl_{1-x}Br_x, BiOCl_{1-x}I_x, and BiOBr_{1-x}I_x alloy systems. Using density functional theory calculations combined with the generalized quasichemical approximation, we systematically investigated band gaps and density of states for all symmetrically non-equivalent configurations in 24-atom supercells. Our calculations reveal significant band gap bowing behavior with bowing parameters of 0.98, 2.23, and 2.70 eV for BiOCl_{1-x}Br_x, BiOBr_{1-x}I_x, and BiOCl_{1-x}I_x alloys, respectively, representing substantial deviations from Vegard's law. Point defect formation energy calculations demonstrate that although halogen substitution is endothermic, the formation energies remain sufficiently low (2–143 meV per dopant atom) to enable experimental synthesis. The mixing enthalpies remain below 10 meV per formula unit across the entire composition range for all three systems. At typical synthesis temperatures, the configurational entropy contribution easily overcomes the enthalpy penalty, stabilizing the random solid solution. We successfully synthesized BiOCl_{1-x}I_x nanoparticles across the complete composition range (x = 0–1) with yields exceeding 90%, experimentally validating our predictions. UV-visible spectroscopy of the synthesized alloys confirms the predicted red-shift in absorption onset with increasing iodine content. While the electronic band structures exhibit strong bowing effects, the absorption spectra are reasonably captured by a linear interpolation between pure end-members, providing a practical approximation for targeted optical design applications. The minimum band gaps occur at approximately 75–78% heavier halogen content, offering optimal visible light absorption. These findings provide fundamental insights into halogen alloying mechanisms in bismuth oxyhalides and establish clear design principles for enhanced photo-absorption or photo-catalytic applications.

 Received 19th December 2025,
 Accepted 22nd May 2026

DOI: 10.1039/d5cp04955e

rsc.li/pccp

1. Introduction

Bismuth oxyhalides (BiOX, where X represents Cl, Br, and I) have been considered for diverse applications spanning electronics, energy conversion, energy storage, and environmental remediation.^{1–4} Among them, the BiOCl system has demonstrated exceptional photocatalytic activity, as substantiated by extensive research.^{5–7} The structure of BiOCl exhibits a distinctive nanoplate morphology featuring alternating Bi₂O₂ layers intercalated with double-layer Cl slabs, as illustrated in Fig. 1. Previous density functional theory (DFT) calculations have

classified this compound as an indirect band gap semiconductor.⁸ The valence band (VB) is primarily composed of O-2p and Cl-3p orbitals, while the conduction band (CB) predominantly consists of Bi-6p orbitals. Upon photoexcitation, electrons transition from Cl-3p orbitals to hybridized Bi-6p-derived bands, resulting in distinctive photocatalytic properties.⁸ However, the photocatalytic efficiency of BiOCl is constrained by its relatively wide band gap (3.02–3.5 eV^{9,10}) and indirect nature, which limits visible light absorption and restricts activity primarily to the UV range.

Fortunately, the layered structure of BiOCl provides multiple opportunities for band gap engineering through morphology control,¹¹ hetero-junction formation,¹² and impurity doping.¹³ A particularly promising strategy for band gap tuning is halogen anion alloying.^{14–16} The chemical similarity among halogens facilitates the synthesis of solid solutions such as BiOCl_{1-x}I_x,¹⁷ BiOCl_{1-x}Br_x,¹⁸ and BiOBr_{1-x}I_x.¹⁹

^a Research Center Future Energy Materials and Systems of the University Alliance Ruhr and Interdisciplinary Centre for Advanced Materials Simulation, Ruhr University Bochum, Universitätsstraße 150, D-44801, Bochum, Germany.
 E-mail: miguel.marques@rub.de

^b L'Oréal Research and Innovation, 93601, Aulnay sous Bois, France



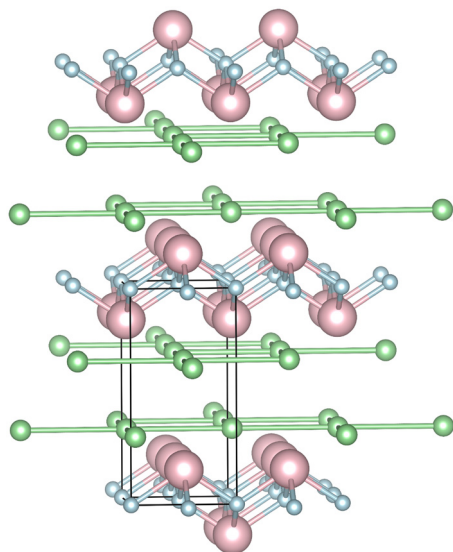


Fig. 1 The crystal structure of BiOCl. The pink, light blue, and green spheres denote the Bi, O, and Cl atoms, respectively.

Previous DFT investigations have demonstrated that anion alloying can dramatically reduce the band gap of BiOBr,²⁰ BiOCl,²¹ and BiOF.²² The variation of band gap with respect to anion ratios in anion mixed structures was investigated and large band gap bowing behavior was found.²³ However, these studies employed single ordered configurations (typically in $2 \times 2 \times 1$ supercells) for each stoichiometry. This single-configuration approach cannot capture the distribution of local environments in a truly disordered solid solution, which is essential for describing the properties of experimentally synthesized alloys.

To properly account for configurational disorder in alloys, several theoretical approaches have been developed, each with distinct advantages and limitations. The special quasirandom structure (SQS) model²⁴ is widely employed to identify representative atomic configurations that reproduce the pair and multi-site correlation functions characteristic of random alloys. While SQS structures are amenable to standard DFT calculations, this approach suffers from important limitations: (i) it typically represents the alloy through a single supercell or a small set of configurations, providing only point estimates rather than proper thermodynamic ensemble averages; (ii) results depend critically on user-defined choices such as correlation functions to be matched and the supercell size; and (iii) it does not readily yield information about property distributions across different configurations. Coherent potential approximation (CPA)²⁵ adopts a complementary strategy, treating disorder through a self-consistent mean-field approach wherein the random alloy is replaced by an effective ordered medium with composition-dependent potentials. While CPA offers computational efficiency and captures disorder-induced effects on the average electronic structure, it inherently sacrifices information about specific local atomic environments, their energetic distributions, and property fluctuations arising from compositional variations. Virtual crystal approximation

(VCA)²⁶ represents the simplest approach, treating the alloy composition as a continuous variable through linear interpolation of atomic potentials between end-members. Although VCA provides qualitative trends with a minimal computational cost, it fundamentally neglects the discrete nature of atomic substitutions and typically underestimates band gap bowing by failing to capture the nonlinear responses to local compositional variations. In contrast, generalized quasichemical approximation (GQCA)^{27,28} explicitly enumerates all symmetrically non-equivalent atomic configurations within a finite supercell and weights their contributions according to formation energies through a temperature-dependent Boltzmann distribution. This approach combines the rigor of explicit configuration enumeration with proper thermodynamic ensemble averaging, making it particularly suitable for simulating disordered solid solutions. Moreover, GQCA naturally provides access to both average properties and their distributions across different configurations at each composition, which can be crucial for understanding experimental variability and predicting synthesis outcomes.

In this study, we combine density functional theory (DFT) calculations with GQCA to systematically investigate the electronic and optical properties of BiOCl_{1-x}Br_x, BiOCl_{1-x}I_x, and BiOBr_{1-x}I_x disordered solid solutions. We address three key aspects that remain poorly understood in these systems. First, we investigate the formation energies of the solid solution with respect to the pristine parent compounds and establish quantitative relationships between theoretical predictions and experimental synthesis feasibility across the complete composition range. Second, we systematically compare band gap bowing behavior and its compositional dependence across all three alloying systems, revealing how different halogen combinations influence the electronic structure through rigorous configurational averaging. Third, we examine optical absorption spectra from both theoretical and experimental perspectives, establishing the connection between electronic band structure bowing and practical optical properties relevant for photo-absorption applications.

II. Methods

II.A. DFT calculation

We performed all geometry optimizations and total energy calculations using the code VASP.^{29,30} We used the projector augmented wave setups^{31,32} of VASP version 5.2 with a cutoff of 520 eV. We used uniform Γ -centered k -point grids to sample the Brillouin zones with densities of 2000 and 3000 k -points per reciprocal atom for geometry optimizations and total energy calculations, respectively. We used the Perdew–Burke–Ernzerhof (PBE)³³ exchange–correlation functional in all calculations. Spin–orbit coupling (SOC) was included in all calculations given the presence of the heavy element Bi ($Z = 83$), whose relativistic effects influence the band structure by splitting of the Bi-6p-derived conduction bands.³⁴ As shown in Table S1 of the SI, the inclusion of SOC leads to significant differences relative to scalar-relativistic calculations, most notably for the BiOCl_{1-x}I_x



Table 1 Calculated cell parameters and band gaps for pristine BiOX (X = Cl, Br, and I) structures

	BiOCl	BiOBr	BiOI
<i>a</i> (Å)	3.908 (3.874 ^a , 3.905 ^b , 3.87 ^c , 3.89 ^d)	3.947 (3.900 ^a , 3.90 ^c , 3.93 ^d)	4.028 (3.968 ^a , 4.035 ^b , 3.98 ^c , 4.00 ^d)
<i>c</i> (Å)	7.998 (7.367 ^a , 7.87 ^b , 7.42 ^c , 7.49 ^d)	8.912 (8.325 ^a , 8.14 ^c , 8.39 ^d)	9.977 (9.380 ^a , 9.27 ^b , 9.15 ^c , 9.60 ^d)
Gap (eV)	2.61 (2.49 ^a , 2.90 ^b , 3.37 ^c , 2.57 ^d)	2.25 (2.15 ^a , 2.82 ^c , 2.27 ^d)	1.50 (1.59 ^a , 1.57 ^b , 2.00 ^c , 1.48 ^d)

^a Reference data using PBEsol.²³ ^b Reference data using PBE + DFT-D3.²¹ ^c Reference data using HSE06.³⁴ ^d Reference data using r2SCAN.³⁶

system, underlining the importance of treating relativistic effects in these heavy-element compounds. We converged the forces to values smaller than 0.005 eV Å⁻¹ during optimization, and for total energy calculation, we converged the energy below 0.01 meV per atom. The frequency-dependent dielectric function was calculated within the independent-particle approximation (IPA).³⁵

To validate our computational approach, Table 1 compares the calculated structural parameters and band gaps of pristine BiOCl, BiOBr, and BiOI with reference values from the literature obtained with different exchange–correlation functionals. Our PBE results are in good agreement with previous calculations. Minor differences can be attributable to the choice of functional.

The average properties of the alloys were obtained using a thermodynamic ensemble average within the GQCA.^{27,28} Within this approximation, a macroscopic N atom disordered cell can be represented by the total number of *M* cluster cells, with *n_i* atomic alloying sites in each cluster. The cluster cells can be grouped into *J* different classes, with each class containing all degenerate (equivalent according to their space group symmetry) clusters. All classes (*M_j*) together with their cluster fraction *x_j* form a set {(*M_j*, *x_j*) | *j* = 1, ..., *J*} that fully describes the macroscopic disordered alloy.

Fraction *x_j* depends on the energy per atom (*E_j*), the symmetry degeneracy (*g_j*), and the atomic fraction of two alloying systems A and B (*c_j*) through

$$x_j = \frac{g_j \eta_j \exp(-\beta \Delta E_j)}{\sum_k g_k \eta_k \exp(-\beta \Delta E_k)} \quad (1)$$

$$\Delta E_j = E_j - c_j E_A - (1 - c_j) E_B, \quad (2)$$

where $\beta^{-1} = k_B T$. The coefficient η_j is found by minimization of the Helmholtz free energy with the constraints

$$\sum_j x_j = 1, \quad \sum_j c_j x_j = c_A, \quad (3)$$

where *c_A* is the molar concentration of pure system A in the macroscopic alloy. Any composition-dependent property *P* (*c_A*) is then obtained using the Connolly–Williams statistical average³⁷ of the corresponding properties *P_j* over all *J* classes:

$$P(c_A) = \sum_j x_j P_j. \quad (4)$$

The supercell geometries were generated using 17 inequivalent transformation matrices **M** satisfying $\det(\mathbf{M}) \leq 4$,

yielding simulation cells of up to 24 atoms. The number of halogen atoms in each supercell is $x \times \det(\mathbf{M}) \times 2$ (reflecting two halogen sites per primitive unit cell), where *x* is restricted to rational values consistent with the supercell size. All possible colorings of the halogen pairs onto the supercell sites were enumerated and symmetry-equivalent duplicates were removed, resulting in 437 distinct configurations across all compositions and supercell sizes. The dependence of the GQCA results on the supercell size is expected to be small: previous studies on similar BiOX systems using a single $2 \times 2 \times 1$ supercell^{20–22} found well-converged results, owing to the weak interlayer halogen–halogen interactions. All optimized structures are included in the SI.

II.B. Syntheses

All materials were used without specific purification. Bi(NO₃)₃·5H₂O (purity: 98%), potassium chloride (purity: 99%) and D-mannitol (purity: 98%) were purchased from Sigma-Aldrich. Potassium iodide (purity: 99%) was purchased from Carlo Erba Reactifs. In a typical experiment, a 100 mL solution with 1.94 g of Bi(NO₃)₃·5H₂O and 2.0 g of D-mannitol was prepared using ultrasonication to facilitate the dissolution. Just after dissolution, this solution was poured in a 250 mL flask and a 10 mL KCl solution was added, resulting in a white precipitate. A third solution containing KI was then added (10 mL), resulting in coloration. Potassium chloride and potassium iodide quantities were adjusted to fit the I/Cl ratio ($x = n_I/(n_I + n_{Cl})$) and the stoichiometry of the composition ($n_I + n_{Cl} = n_{Bi}$). The values of *x* were chosen among {0, 0.05, 0.1, 0.25, 0.5, 1}. The medium was then heated under stirring at 100 °C (reflux) for 6 hours and the medium was maintained under stirring to cool to room temperature. At the end of the reaction, the medium was a white to orange suspension depending on the I/Cl ratio. The material was separated using centrifugation at 4000 rpm, washed twice with water and dried under vacuum at 60 °C to obtain white to orange powders of BiOCl_{1-x}I_x nanoparticles, with yields typically above 90%.

II.C. UV-visible spectrophotometry

Dispersions with 0.1 wt% of bismuth oxyhalides (BiOCl_{1-x}I_x) were prepared in a water/propylene glycol/polysorbate 20 (Tween 20) mixture with respective weight fractions of 49.85/49.85/0.30. The dispersions were sonicated for 15 min and then stirred with a magnetic stirrer for 16 h. The suspensions were then diluted to 0.01 wt% in bismuth oxyhalides (BiOCl_{1-x}I_x) with the same medium and stirred again with magnetic stirring for 20 min. For each spectrum, around 2.5 mL of the 0.01 wt% dispersion was placed in a quartz cell (1 cm optical path



length). The UV-vis spectrum was then collected between 220 and 800 nm using a Genesys 10S spectrophotometer (Thermo Fisher Scientific).

III. Results and discussion

III.A. Defect formation energies

We calculated the single point-defect formation energies using the following expression:

$$\Delta E_f = E(\text{BiOX:Y}_x^\times) - E(\text{BiOX}) + E(\text{X}) - E(\text{Y}) \quad (5)$$

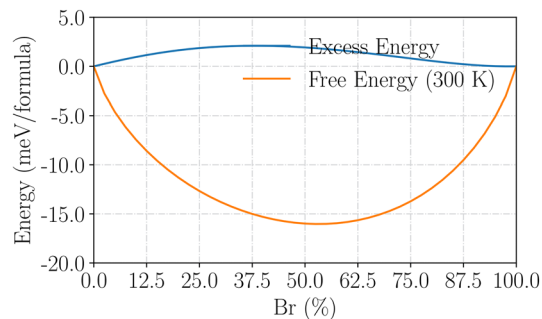
where the energies of the X (substituted) and Y (dopant) atoms correspond to the total energy per atom for the most stable pure elementary halogen solids at 0 K. Our calculations reveal that substitutional defect formation is endothermic for all doping systems investigated (see Table 2). However, for Br substituting Cl the formation energy is remarkably low, being only several millielectronvolts per defect. This minimal energy requirement suggests negligible thermodynamic obstacles for achieving Br–Cl alloying under experimental conditions. In contrast, iodine doping exhibits significantly higher substitution energies (approximately 100 meV per dopant atom) compared to bromine doping. Nevertheless, when compared to other anion-alloying systems reported in the literature, *e.g.* $\text{Cs}_2\text{AgBiBr}_{6-x}\text{Cl}_x$,¹⁴ the formation energy is still one order of magnitude lower. These energetic considerations indicate that halogen substitution and solid-solution formation in $\text{BiOX}_{1-x}\text{Y}_x$ systems are synthetically feasible.

To assess the full thermodynamic stability of the solid solutions beyond the dilute limit, we calculated the mixing enthalpy and Helmholtz free energy at 300 K for all three alloy systems within the GQCA framework, as shown in Fig. 2. The mixing enthalpies remain below 10 meV per formula unit across the entire composition range for all three systems. For $\text{BiOBr}_{1-x}\text{I}_x$ the mixing is even slightly exothermic. At typical synthesis temperatures, the configurational entropy contribution easily overcomes the enthalpy penalty, stabilizing the random solid solution, as confirmed by the negative Helmholtz free energy curves in Fig. 2. Importantly, none of the three systems exhibit inflection points in the free energy curve at 300 K, confirming the absence of a miscibility gap and ruling out spontaneous phase separation under experimental conditions. The successful experimental synthesis of $\text{BiOCl}_{1-x}\text{I}_x$ with the highest mixing enthalpy among the three with yields exceeding 90% provides direct experimental validation of this thermodynamic analysis.

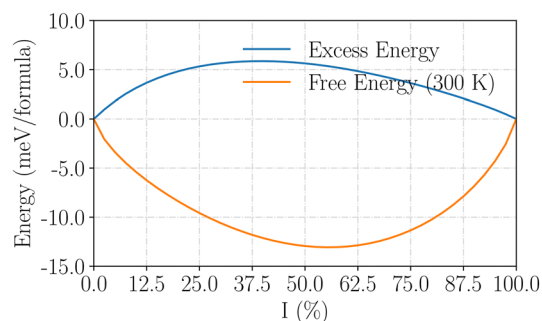
To validate our computational predictions regarding the thermodynamic feasibility of $\text{BiOCl}_{1-x}\text{I}_x$ alloys, we successfully synthesized a series of nanoparticles with varying iodine concentrations ($x = 0, 0.05, 0.1, 0.25, 0.5, \text{ and } 1.0$). The successful

Table 2 The point defect formation energies (E_f , in meV/defect) for the BiOX systems

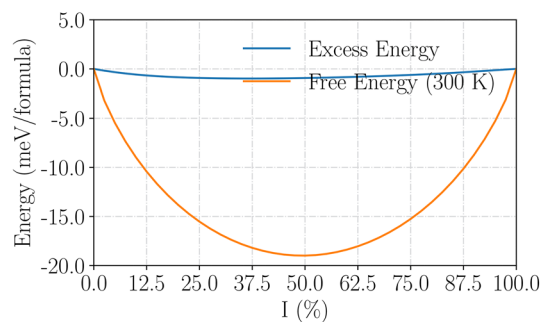
Defect _{Lattice} ^{Charge}	$\text{Br}_{\text{Cl}}^\times$	$\text{I}_{\text{Cl}}^\times$	$\text{I}_{\text{Br}}^\times$
ΔE_f	2	143	135



(a)



(b)



(c)

Fig. 2 Mixing enthalpy (excess energy) and Helmholtz free energy at 300 K as a function of composition for (a) $\text{BiOCl}_{1-x}\text{Br}_x$, (b) $\text{BiOCl}_{1-x}\text{I}_x$, and (c) $\text{BiOBr}_{1-x}\text{I}_x$.

synthesis across this entire composition range experimentally confirms our theoretical prediction that halogen substitution in BiOX systems is synthetically feasible from an energetic perspective, despite the endothermic nature of the substitution process. The experimental synthesis yields were consistently above 90% for all compositions, indicating efficient alloy formation. This high yield is consistent with our calculated point defect formation energies, which showed that while I–Cl substitution requires approximately 143 meV per defect, this energy barrier remains one order of magnitude lower than other mixed-anion systems such as perovskites, making the synthesis experimentally accessible.

III.B. Alloying effect on band gaps

We further calculated the band gaps for $\text{BiOCl}_{1-x}\text{Br}_x$ anion-alloys with Br concentrations ranging from 0 to 1 with



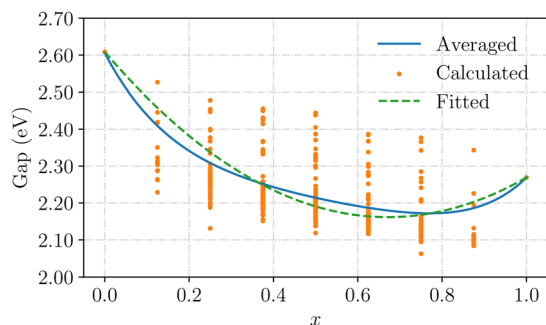


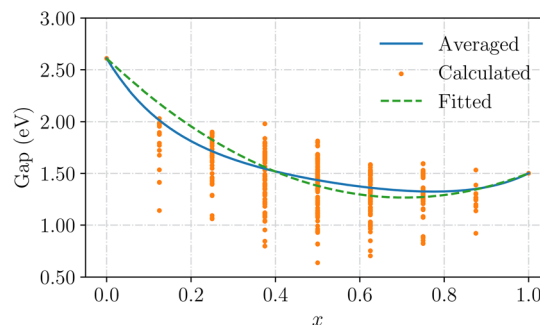
Fig. 3 The band gaps vary as a function of the Br ratio in the $\text{BiOCl}_{1-x}\text{Br}_x$ alloy. The dots correspond to the calculated gaps for different configurations, the blue line shows the thermodynamically averaged gap varying with the ratio of Br (x), and the green line shows the fitted curve according to eqn (6).

increments of 0.125, and the results are presented in Fig. 3. For the alloyed systems, the band gaps remain indirect, similar to those of the parent pristine BiOCl and BiOBr . For each Br concentration, we consider all non-equivalent configurations of Br substitution in a 24-atom supercell. The calculated band gap values exhibit a distribution spanning approximately 0.3 eV, with a greater number of configurations displaying lower band gaps compared to higher band gaps at each composition ratio. The most significant finding in our analysis is the distinctive bowing behavior exhibited by the averaged band gap curve. This band gap bowing effect, as observed in our study, represents a common phenomenon in semiconductor alloys and bears resemblance to similar behaviors reported in other alloy systems,³⁸ including $\text{Be}_x\text{Zn}_{1-x}\text{Se}$ ³⁹ and alkaline earth chalcogenides.⁴⁰

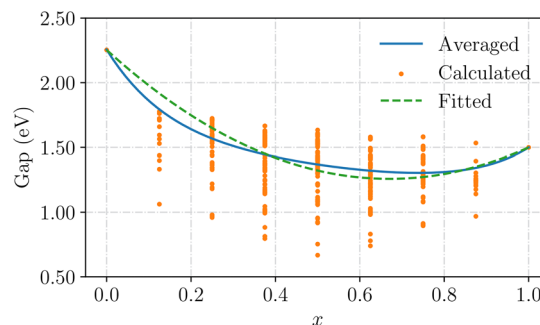
Band gap bowing represents a departure from Vegard's law⁴¹ which predicts a linear interpolation between the pure end-member systems. Instead, the band gap of an alloy A_xB_{1-x} can be described by the following expression:

$$E_g(x) = xE_g(\text{A}) + (1-x)E_g(\text{B}) - bx(1-x), \quad (6)$$

where b represents the band gap bowing parameter.³⁸ For $\text{BiOCl}_{1-x}\text{Br}_x$ alloys, we determined a bowing parameter of 0.98 eV, with the alloy achieving a minimum band gap of 2.17 eV when 77% of Cl atoms are replaced by Br. Furthermore, our findings reveal a rapid decrease in band gap values even with minimal Br incorporation. This demonstrates the high sensitivity of the electronic band structure to Br incorporation, enabling significant tunability in the band structure through even a low doping concentration. This sensitivity provides valuable opportunities for tuning optoelectronic behavior of $\text{BiOCl}_{1-x}\text{Br}_x$. Near the minimum E_g ($x \approx 0.77$), the band gap variation exhibits a relatively gradual response to Br/Cl ratio changes. This behavior suggests that around $x = 0.77$ the electronic structure maintains a degree of stability with respect to the varying chemical stoichiometry of the alloy. It should be noted that eqn (6) captures the dominant bowing behavior but cannot fully reproduce the observed nonlinearity, as the fitted curves show small deviations from the thermodynamically averaged values.



(a)



(b)

Fig. 4 The band gaps vary as a function of the I ratio in the (a) $\text{BiOCl}_{1-x}\text{I}_x$ and (b) $\text{BiOBr}_{1-x}\text{I}_x$ alloys. The dots correspond to the calculated gaps for different configurations, the blue line shows the thermodynamically averaged gap varying with the ratio of I (x), and the green line shows the fitted curve according to eqn (6).

As illustrated in Fig. 4, similar band gap bowing effects are observed in $\text{BiOCl}_{1-x}\text{I}_x$ and $\text{BiOBr}_{1-x}\text{I}_x$ alloys, where the minimal gaps are found at 78% and 74% iodine ratios, respectively. Similar to the previous cases, the band gaps of the alloyed systems remain indirect. However, these systems exhibit significantly larger bowing parameters of 2.70 and 2.22 eV, respectively.

Band-gap bowing in semiconductor alloys generally originates from two contributions^{42–44}: (i) the chemical effect (CE), arising from electrostatic potential fluctuations induced by the mixing of chemically distinct atoms; and (ii) the geometry effect (GE), arising from structural distortions (both local and cell-level deformation) due to the size mismatch between the alloying species. In BiOX alloys, the lattice mismatch between BiOCl , BiOBr , and BiOI is particularly large, especially along the interlayer c direction, suggesting that the geometry effect should dominate, as observed in other highly mismatched semiconductor alloys.⁴² The calculated band gaps of pure BiOCl and BiOI (see Fig. S1 in the SI) indeed vary non-linearly with lattice parameter c .

To quantitatively test this hypothesis, we performed a decomposition analysis on the $\text{BiOCl}_{0.25}\text{I}_{0.75}$ composition, which is close to the composition giving the minimal gap of the alloy system. We computed the band gaps of pure BiOCl and BiOI structures adapted to the distorted $\text{BiOCl}_{0.25}\text{I}_{0.75}$



geometries, yielding “intermediate pure phases”. The average gaps of these distorted BiOCl and BiOI structures are 1.64 and 1.17 eV, respectively. The linear interpolation ($x = 0.75$) between them is 1.29 eV, fairly close to the actual average gap of this composition (1.28 eV). This means that the non-linearity of band bowing mainly originates from geometry distortion of the pure phases when alloying. This confirms that the geometry effect accounts for the dominant fraction of the band gap variation and the deviation from Vegard’s law, with the chemical effect playing only a minor role.

The magnitude of the bowing parameters follows the expected correlation with the ionic size and electronegativity mismatch between the halogen pairs.⁴⁵ Typical III–V semiconductors with cation mixing exhibit bowing parameters below 0.2 eV for closely matched systems (*e.g.*, GaAs–AlAs) and above 1 eV for highly mismatched ones.⁴⁶ Anion-mixed systems generally show larger values: zinc blende anion-mixed alloys span approximately 0.5–4 eV depending on the degree of mismatch,^{45–47} and mixed chalcogenide systems such as ZnS_{1–x}Te_x can reach 2–3 eV due to the large S–Te size difference.⁴⁷ In our BiOX_{1–x}X’_x alloys, the mismatch is largest between Cl and I (ionic radii: 1.81 vs. 2.20 Å; electronegativity: 3.16 vs. 2.66 Pauling) and smallest between Br and I (ionic radii: 1.96 vs. 2.20 Å; electronegativity: 2.96 vs. 2.66), consistent with the order BiOCl_{1–x}I_x (2.70 eV) > BiOBr_{1–x}I_x (2.23 eV) > BiOCl_{1–x}Br_x (0.98 eV).

We acknowledge that the PBE functional systematically underestimates absolute band-gap values. However, this limitation does not significantly affect the bowing parameter, which characterizes the curvature of the composition dependence (eqn (6)) rather than the absolute band-gap values at a given stoichiometry. Since PBE yields a nearly uniform underestimation across the chemically similar BiOX compounds, this systematic error largely cancels when computing *b*, as demonstrated in prior studies on semiconductor alloys.^{46,48}

To further investigate the electronic structure of the alloys, we plotted the averaged and normalized density of states (DOS)

for BiOCl_{1–x}I_x alloys. As shown in Fig. 5, the DOS of the alloys deviates from the linear interpolation between two pure systems. With increasing iodine concentration in the alloys, the DOS of the CBs and higher-energy VBs increases, while the changes in the lower-energy VBs do not follow a monotonic trend. More interestingly, both pure BiOCl and BiOI exhibit lower DOS values near the Fermi level (E_f) compared to their alloy counterparts. This increased density around E_f could be potentially beneficial for achieving enhanced optical absorption.

III.C. Optical absorption

We investigated the alloying effects on the absorption of UV photons by calculating the absorption spectra under the independent-particle approximation (IPA).³⁵ To limit computational cost, we calculated the averaged spectra for low-energy configurations of BiOI_{0.125}Cl_{0.875} and BiOI_{0.25}Cl_{0.75} alloys. The results are presented in Fig. 6. Consistent with the above electronic structure results, the onset is red-shifted for the alloys. The higher iodine concentration ($x = 0.25$) results in a lower onset energy and enhanced absorption in the photon energy range below 2 eV. Remarkably, despite different cluster configurations possess distinct geometries and consequently different energies and electronic structures, absorption spectra remain nearly identical across configurations at a given iodine concentration. One of the reasons could be that the onset is largely aligned with the low energy CBs from I–p states. Partially due to this, the spectra of the alloys can be well approximated by a linear interpolation between the two pure end-member systems, particularly in the lower energy range (below 320 nm) (see dotted lines in Fig. 6(a)). This finding implies that for the mixed-anion BiOX systems, the linearly interpolated absorption spectra can be used to narrow down the target onset before experimental syntheses.

It is important to address the relationship between the electronic band gap bowing (Fig. 3 and 4) and the nearly linear behavior observed in the absorption spectra (Fig. 6(a)). While

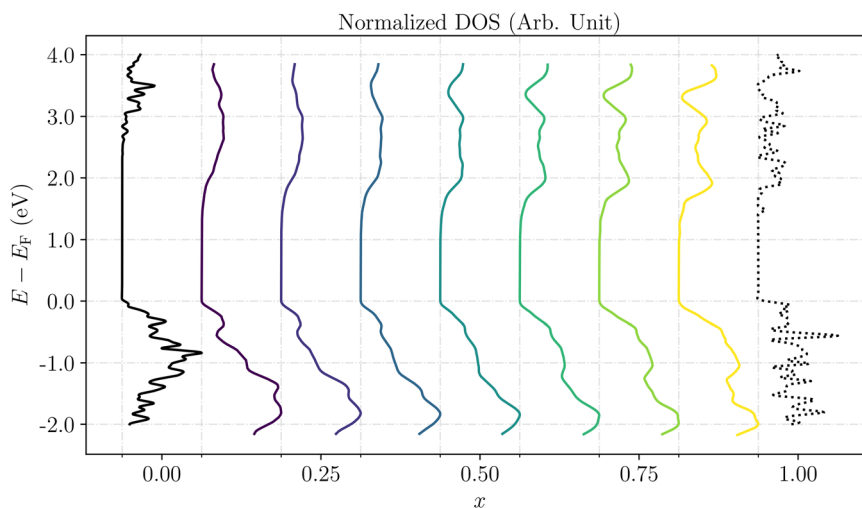


Fig. 5 The averaged density of states (around the Fermi level) in the BiOCl_{1–x}I_x alloys. The density of states for pure BiOCl and BiOI are plotted as black solid and dotted lines, respectively.



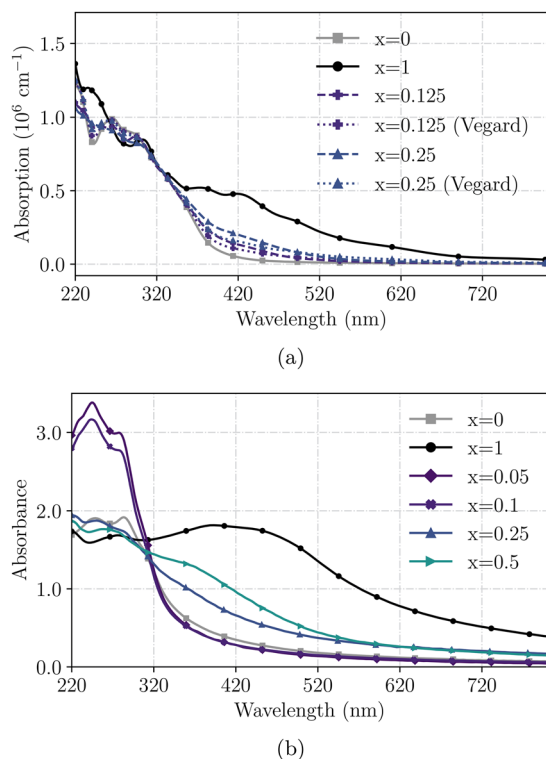


Fig. 6 (a) Averaged absorption coefficient for $\text{BiOCl}_{0.875}\text{I}_{0.125}$ and $\text{BiOCl}_{0.75}\text{I}_{0.25}$ alloys calculated at the IPA level and (b) measured absorbance of $\text{BiOCl}_{1-x}\text{I}_x$ nanoparticles dispersed in a hydrophilic medium (H_2O -propylene glycol-Tween 20) at 0.01 wt%. Note that the comparison is limited to the onset position and spectral shape, not absolute intensities.

the electronic band gaps exhibit strong non-monotonic composition dependence, the absorption spectra follow approximately linear interpolation between the pure end-members. This apparent difference arises because optical absorption is determined by optical transition matrix elements integrated over the entire Brillouin zone, not solely by the valence maxima to conduction minima transitions. This momentum-space averaging smooths out the sharp compositional variations present at the band edges, resulting in absorption spectra that vary more gradually with composition than the fundamental band gaps. Furthermore, we acknowledge that the PBE functional systematically underestimates band gaps, causing our calculated absorption onsets to be red-shifted compared to experimental values. However, this error manifests as an approximately rigid shift that does not affect the relative trends, compositional ordering, or the key finding that absorption spectra can be approximated by linear interpolation. Previous studies have demonstrated that semi-local functionals reliably reproduce bowing parameters and spectral trends in semiconductor alloys despite underestimating absolute band gap values.^{23,49–51} Our comparison with experimental UV-visible spectra (Fig. 6(b)) confirms that after accounting for the systematic shift, the variation trends of calculated absorption across compositions are in excellent agreement with measurements.

Fig. 6(b) presents the experimental UV-visible absorption spectra of the synthesized $\text{BiOCl}_{1-x}\text{I}_x$ nanoparticles, which

provide direct validation of our computational predictions. The experimental results demonstrate several key findings that align remarkably well with our theoretical calculations. Firstly, the experimental spectra clearly show a progressive red-shift in the absorption onset with increasing iodine content, moving from the UV for pure BiOCl toward the visible range for iodine-rich compositions. This trend directly validates our computational prediction of decreasing band gaps with increasing iodine concentration. Secondly, the experimental absorption spectra exhibit smooth, gradual changes with composition that closely follow the linear interpolation behavior predicted by our calculations. This experimental validation confirms our theoretical finding that, despite the strong band gap bowing in the electronic structure, the absorption spectra can be reasonably approximated by a linear interpolation between the pure end-members. Finally, the experimental absorption edge positions show excellent agreement with our calculated band gap values when accounting for the typical differences between optical and electronic band gaps. For instance, the experimental spectrum for $x = 0.25$ shows an absorption onset around 450–500 nm (2.5–2.8 eV), which is in alignment with our calculated onset.

We have to emphasize that the calculated optical absorption spectra should be interpreted recognizing the well-known limitations of semilocal exchange–correlation functionals. In particular, the absorption onset and band-gap-related transition energies are systematically underestimated compared to experimental values. However, previous studies demonstrate that the spectral line shapes, relative peak positions, and compositional trends are described reliably within this level of theory. More advanced treatments, such as many-body GW calculations combined with the Bethe–Salpeter equation (BSE), would be prohibitively expensive for the large supercells required for the GQCA-based configurational enumeration.

IV. Conclusions

Bismuth oxyhalides are layered materials representing a promising platform for developing safe, environment-friendly, sustainable and versatile UV absorbing materials. We systematically investigated how halogen anion alloying affects the electronic structures and optical properties of BiO (I, Br, and Cl) systems. From an energetic perspective, we determined that substituting Cl with Br requires minimal energy, and the substitution energies for replacing Br or Cl with I are higher but remain one order of magnitude smaller compared to those of other mixed-anion systems such as perovskites. This indicates that BiOXY alloys can be readily synthesized experimentally. We further calculated the band gaps and density of states for all symmetrically non-equivalent clusters containing fewer than 24 atoms. The results demonstrate that the thermodynamically averaged band gap values and DOS significantly deviate from linear interpolation based on Vegard's law. The minimum band gaps are observed at heavy/light halogen atom ratios of approximately 75%. Additionally, we calculated the absorption spectra for low-energy configurations of $\text{BiOCl}_{1-x}\text{I}_x$ within the



independent-particle approximation. We found that despite strong deviations of alloy electronic structures from Vegard's law, the absorption spectra can be well-approximated by linear interpolation between the pure end-members. The combined computational and experimental results provide valuable insights for applications. Our calculations predict that the minimum band gap occurs at approximately 75–78% iodine content across different halogen combinations, which would maximize visible light absorption. However, the experimental synthesis becomes increasingly challenging at high iodine concentrations due to the higher formation energies, suggesting an optimal balance between synthetic feasibility and optical properties. The increased density of states near the Fermi level in the alloys, as revealed by our DOS calculations, combined with the experimentally observed enhanced visible light absorption, suggests that moderate iodine doping ($x = 0.1$ – 0.3) may provide an optimal balance of synthetic accessibility, stability, and photoabsorption. These results support the possibility of theoretically assisting the design of new UV absorbing materials for various applications including heterojunctions, sun filters, photostabilizing agents, etc.

Conflicts of interest

The authors A.V., C.L. and J.G. are employees of the L'Oréal company. The remaining authors declare no conflicts of interest.

Data availability

All relevant data are already included in the manuscript.

Supplementary information (SI) is available. See DOI: <https://doi.org/10.1039/d5cp04955e>.

Acknowledgements

The authors gratefully acknowledge Drs. Julien Hitce and Cynthia Ghobril for helpful discussions and Karine Garnier for her helpful literature survey, as well as L'Oréal R&I for funding the project.

References

- 1 J. Xiong, G. Cheng, F. Qin, R. Wang, H. Sun and R. Chen, Tunable BiOCl hierarchical nanostructures for high-efficient photocatalysis under visible light irradiation, *Chem. Eng. J.*, 2013, **220**, 228.
- 2 S. Jiang, X. Peng, Y. Hu and Z. Gui, Facile synthesis of a rose-like BiOCl assembled from nanosheets and its thermal-property application in polymers, *Mater. Lett.*, 2015, **161**, 561.
- 3 S. Sharma, A. D. Acharya, Bhawna, Y. S. Thakur and S. Bisoyi, Optimizing BiOCl concentration for enhanced LDPE performance: Investigation of structure, thermal stability, and optical characteristics, *J. Mol. Struct.*, 2023, **1294**, 136382.
- 4 M. N. Gordon, K. Chatterjee, N. Christudas Beena and S. E. Skrabalak, Sustainable production of layered bismuth oxyhalides for photocatalytic H₂ production, *ACS Sustainable Chem. Eng.*, 2022, **10**, 15622.
- 5 M. Guan, C. Xiao, J. Zhang, S. Fan, R. An, Q. Cheng, J. Xie, M. Zhou, B. Ye and Y. Xie, Vacancy associates promoting solar-driven photocatalytic activity of ultrathin bismuth oxychloride nanosheets, *J. Am. Chem. Soc.*, 2013, **135**, 10411.
- 6 X. Zhang, Z. Ai, F. Jia and L. Zhang, Generalized onepot synthesis, characterization, and photocatalytic activity of hierarchical BiOX (X = Cl, Br, I) nanoplate microspheres, *J. Phys. Chem. A*, 2008, **112**, 747.
- 7 Y. Wang, Z.-q Shi, C.-m Fan, X.-g Hao, G.-y Ding and Y.-f Wang, Synthesis of BiOCl photocatalyst by a low-cost, simple hydrolytic technique and its excellent photocatalytic activity, *Int. J. Miner., Metall. Mater.*, 2012, **19**, 467.
- 8 W. L. Huang and Q. Zhu, Electronic structures of relaxed BiOX (X = F, Cl, Br, I) photocatalysts, *Comput. Mater. Sci.*, 2008, **43**, 1101.
- 9 J. Henle, P. Simon, A. Frenzel, S. Scholz and S. Kaskel, Nanosized BiOX (X = Cl, Br, I) particles synthesized in reverse microemulsions, *Chem. Mater.*, 2007, **19**, 366.
- 10 H. Deng, J. Wang, Q. Peng, X. Wang and Y. Li, Controlled hydrothermal synthesis of bismuth oxyhalide nanobelts and nanotubes, *Chem. – Eur. J.*, 2005, **11**, 6519.
- 11 S. Kang, R. C. Pawar, Y. Pyo, V. Khare and C. S. Lee, Size-controlled BiOCl-RGO composites having enhanced photodegradative properties, *J. Exp. Nanosci.*, 2015, **11**, 259.
- 12 S. Shamaila, A. K. L. Sajjad, F. Chen and J. Zhang, WO₃/BiOCl, a novel heterojunction as visible light photocatalyst, *J. Colloid Interface Sci.*, 2011, **356**, 465.
- 13 Z. Jiang, F. Yang, N. Luo, B. T. T. Chu, D. Sun, H. Shi, T. Xiao and P. P. Edwards, Solvothermal synthesis of n-doped TiO₂ nanotubes for visible-light-responsive photocatalysis, *Chem. Commun.*, 2008, 6372.
- 14 A. C. Dakshinamurthy, M. Gupta, B. R. K. Nanda and C. Sudakar, Anionic alloying in hybrid halide Cs₂Ag-BiBr_{6-x}Cl_x double perovskites: Is it true alloying or preferential occupation of halide ions in MX₆ octahedra?, *J. Phys. Chem. A*, 2022, **127**, 1588.
- 15 H.-S. Kim, S. H. Jeon, J. S. Park, T. S. Kim, K. S. Son, J.-B. Seon, S.-J. Seo, S.-J. Kim, E. Lee, J. G. Chung, H. Lee, S. Han, M. Ryu, S. Y. Lee and K. Kim, Anion control as a strategy to achieve high-mobility and high-stability oxide thin-film transistors, *Sci. Rep.*, 2013, **3**, 1459.
- 16 S. L. Millican, J. M. Clary, C. J. Bartel, N. R. Singstock, A. M. Holder and C. B. Musgrave, *Alloying behavior of wide band gap alkaline-earth chalcogenides* (2020).
- 17 W. J. Kim, D. Pradhan, B.-K. Min and Y. Sohn, Adsorption/photocatalytic activity and fundamental natures of BiOCl and BiOCl_xI_{1-x} prepared in water and ethylene glycol environments, and Ag and Au-doping effects, *Appl. Catal., B*, 2014, **147**, 711.



- 18 X. Zhang, L. Wang, C. Wang, W. Wang, Y. Chen, Y. Huang, W. Li, Y. Feng and H. Yu, Synthesis of $\text{BiOCl}_x\text{Br}_{1-x}$ nanoplate solid solutions as a robust photocatalyst with tunable band structure, *Chem. – Eur. J.*, 2015, **21**, 11872.
- 19 M. Yadav, S. Garg, A. Chandra and K. Hernadi, Fabrication of leaf extract mediated bismuth oxybromide/oxyiodide ($\text{BiOBr}_x\text{I}_{1-x}$) photocatalysts with tunable band gap and enhanced optical absorption for degradation of organic pollutants, *J. Colloid Interface Sci.*, 2019, **555**, 304.
- 20 H. Huang, X. Li, X. Han, N. Tian, Y. Zhang and T. Zhang, Moderate band-gap-broadening induced high separation of electron-hole pairs in Br substituted BiOI : a combined experimental and theoretical investigation, *Phys. Chem. Chem. Phys.*, 2015, **17**, 3673–3679.
- 21 L. Zhang, Z.-K. Tang, W.-M. Lau, W.-J. Yin, S.-X. Hu and L.-M. Liu, Tuning band gaps and optical absorption of BiOCl through doping and strain: insight from dft calculations, *Phys. Chem. Chem. Phys.*, 2017, **19**, 20968–20973.
- 22 J. Yu, M. Mo, C. Wu, Y. Xiong, J. Wei, R. Zhang and X. Wang, $\text{BiOI}_{0.8-x}\text{F}_{0.2}$ solid solutions with suitable surface halogen vacancies for comprehensive and enhanced photocatalytic performance, *Inorg. Chem.*, 2025, **64**, 16204–16213.
- 23 Z.-Y. Zhao, Q.-L. Liu and W.-W. Dai, Structural, electronic and optical properties of $\text{BiOX}_{1-x}\text{Y}_x$ (X, Y = F, Cl, Br and I) solid solutions from DFT calculations, *Sci. Rep.*, 2016, **6**, 31449.
- 24 A. Zunger, S.-H. Wei, L. G. Ferreira and J. E. Bernard, Special quasirandom structures, *Phys. Rev. Lett.*, 1990, **65**, 353.
- 25 P. Soven, Coherent-potential model of substitutional disordered alloys, *Phys. Rev.*, 1967, **156**, 809.
- 26 L. Bellaiche and D. Vanderbilt, Virtual crystal approximation revisited: Application to dielectric and piezoelectric properties of perovskites, *Phys. Rev. B: Condens. Matter Mater. Phys.*, 2000, **61**, 7877.
- 27 A. Sher, M. van Schilfgaarde, A.-B. Chen and W. Chen, Quasichemical approximation in binary alloys, *Phys. Rev. B: Condens. Matter Mater. Phys.*, 1987, **36**, 4279.
- 28 L. K. Teles, J. Furthmüller, L. M. R. Scolfaro, J. R. Leite and F. Bechstedt, First-principles calculations of the thermodynamic and structural properties of strained $\text{In}_x\text{Ga}_{1-x}\text{N}$ and $\text{Al}_x\text{Ga}_{1-x}\text{N}$ alloys, *Phys. Rev. B: Condens. Matter Mater. Phys.*, 2000, **62**, 2475.
- 29 G. Kresse and J. Furthmüller, Efficiency of ab-initio total energy calculations for metals and semiconductors using a plane-wave basis set, *Comput. Mater. Sci.*, 1996, **6**, 15.
- 30 G. Kresse and J. Furthmüller, Efficient iterative schemes for ab initio total-energy calculations using a plane-wave basis set, *Phys. Rev. B: Condens. Matter Mater. Phys.*, 1996, **54**, 11169.
- 31 P. E. Blöchl, Projector augmented-wave method, *Phys. Rev. B: Condens. Matter Mater. Phys.*, 1994, **50**, 17953.
- 32 G. Kresse and D. Joubert, From ultrasoft pseudopotentials to the projector augmented-wave method, *Phys. Rev. B: Condens. Matter Mater. Phys.*, 1999, **59**, 1758.
- 33 J. P. Perdew, K. Burke and M. Ernzerhof, Generalized gradient approximation made simple, *Phys. Rev. Lett.*, 1996, **77**, 3865.
- 34 A. M. Ganose, M. Cuff, K. T. Butler, A. Walsh and D. O. Scanlon, Interplay of orbital and relativistic effects in bismuth oxyhalides: BiOF , BiOCl , BiOBr , and BiOI , *Chem. Mater.*, 2016, **28**, 1980pMID: 27274616.
- 35 F. Bechstedt, *Many-Body Approach to Electronic Excitations: Concepts and Applications*, Springer, Berlin, Heidelberg, 2015.
- 36 A. Jain, S. P. Ong, G. Hautier, W. Chen, W. D. Richards, S. Dacek, S. Cholia, D. Gunter, D. Skinner, G. Ceder and K. A. Persson, Commentary: The materials project: A materials genome approach to accelerating materials innovation, *APL Mater.*, 2013, **1**, 011002.
- 37 J. W. D. Connolly and A. R. Williams, Densityfunctional theory applied to phase transformations in transition-metal alloys, *Phys. Rev. B: Condens. Matter Mater. Phys.*, 1983, **27**, 5169.
- 38 T. Sandu and R. I. Iftimie, Bandgaps and band bowing in semiconductor alloys, *Solid State Commun.*, 2010, **150**, 888.
- 39 M. Ameri, D. Rached, M. Rabah, F. El Haj Hassan, R. Khenata and M. Doui-Aici, First principles study of structural and electronic properties of $\text{BexZn}_{1-x}\text{S}$ and $\text{BexZn}_{1-x}\text{Te}$ alloys, *Phys. Status Solidi B*, 2008, **245**, 106.
- 40 S. L. Millican, J. M. Clary, C. J. Bartel, N. R. Singstock, A. M. Holder and C. B. Musgrave, *Alloying behavior of wide band gap alkaline-earth chalcogenides*, 2020.
- 41 L. Vegard, Die konstitution der mischkristalle und die raumfüllung der atome, *Z. Phys.*, 1921, **5**, 17.
- 42 T. Sandu and R. I. Iftimie, Bandgaps and band bowing in semiconductor alloys, *Solid State Commun.*, 2010, **150**, 888–892.
- 43 Q. Gao, H. Sahin, J. Kang and S.-H. Wei, Origin of anomalous band-gap bowing in two-dimensional tin-lead mixed perovskite alloys, *Phys. Rev. B: Condens. Matter Mater. Phys.*, 2021, **104**, 064204.
- 44 M. Ferhat and F. Bechstedt, First-principles calculations of gap bowing in $\text{In}_x\text{Ga}_{1-x}\text{N}$ and $\text{In}_x\text{Al}_{1-x}\text{N}$ alloys: Relation to structural and thermodynamic properties, *Phys. Rev. B: Condens. Matter Mater. Phys.*, 2002, **65**, 075213.
- 45 C. S. Schnohr, Compound semiconductor alloys: From atomic-scale structure to bandgap bowing, *Appl. Phys. Rev.*, 2015, **2**, 031304.
- 46 S.-H. Wei, S. B. Zhang and A. Zunger, First-principles calculation of band offsets, optical bowings, and defects in CdS , CdSe , CdTe , and their alloys, *J. Appl. Phys.*, 2000, **87**, 1304–1311.
- 47 I. Vurgaftman, J. R. Meyer and L. R. Ram-Mohan, Band parameters for III-V compound semiconductors and their alloys, *J. Appl. Phys.*, 2001, **89**, 5815–5875.
- 48 C.-Y. Moon, S.-H. Wei, Y. Z. Zhu and G. D. Chen, Band-gap bowing coefficients in large size-mismatched II-VI alloys: first-principles calculations, *Phys. Rev. B: Condens. Matter Mater. Phys.*, 2006, **74**, 233202.



- 49 A. Goyal, S. McKechnie, D. Pashov, W. Tumas, M. van Schilfgaarde and V. Stevanović, Origin of pronounced non-linear band gap behavior in lead–tin hybrid perovskite alloys, *Chem. Mater.*, 2018, **30**, 3920–3928.
- 50 V. Fiorentini and A. Baldereschi, Dielectric scaling of the self-energy scissor operator in semiconductors and insulators, *Phys. Rev. B: Condens. Matter Mater. Phys.*, 1995, **51**, 17196–17198.
- 51 M. Jiang, H. Y. Xiao, S. M. Peng, L. Qiao, G. X. Yang, Z. J. Liu and X. T. Zu, Effects of stacking periodicity on the electronic and optical properties of GaAs/AlAs superlattice: a first-principles study, *Sci. Rep.*, 2020, **10**, 4862.

